From a simple push–pull dye to a broad-band absorbing and photoconducting material by assembly with CuBr

Léo Boivin, Élodie D'astous, Adrien Schlachter, Daniel Fortin, Paul-Ludovic Karsenti, Christophe Lescop, Philippe Dauphin-Ducharme, Pierre Harvey

From a Simple *Push-Pull* Dye to a Broad-Band Absorbing and Photoconducting Material by Assembly with CuBr

Léo Boivin,[1] Élodie V. d'Astous,[1] Adrien Schlachter,[2] Daniel Fortin,[1] Paul-Ludovic Karsenti,[1] Christophe Lescop,[2] Philippe Dauphin-Ducharme,[1] Pierre D. Harvey[1]*

[1]*Département de Chimie, Université de Sherbrooke QC J1K 2R1 Canada*

[2]*Univ Rennes, INSA Rennes, CNRS, ISCR (Institut des Sciences Chimiques de Rennes) – UMR 6226, F-35000 Rennes, France.*

GRAPHICAL ABSTRACT

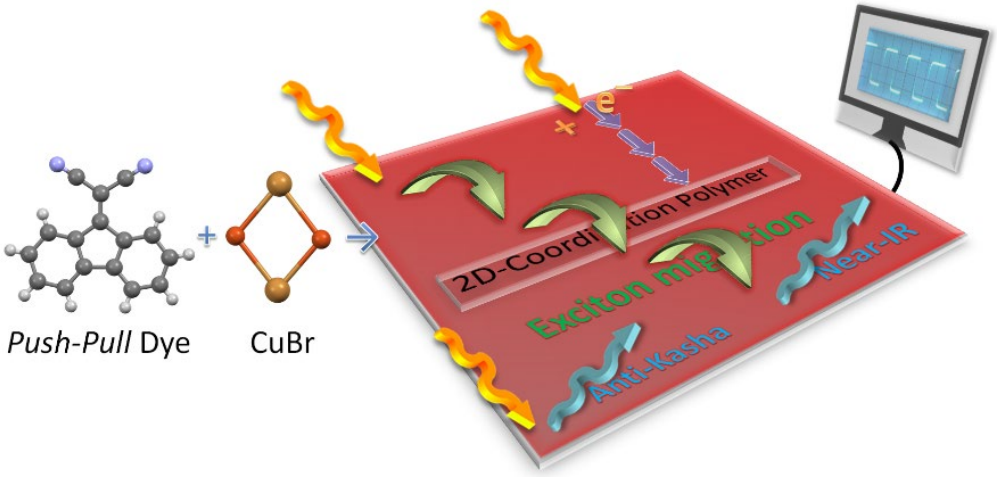

ABSTRACT

A thermally and electrochemically stable 2D coordination polymer (CP) of formula $[Cu_2Br_2\mathbf{L}_2]_n$ (**UDS-6**) has been designed using the *push-pull* chromophore ligand 2-(*9H*-fluorenylidene)malononitrile (**L**) and the modest and yet non-innocent CuBr salt. Its X-ray structure reveals a series of piled 2D-layers separated by ~3.55 Å, inside which π-stacked $\mathbf{L}_2$ pairs are placed in a *head-to-tail* conformation (interplanar **L•••L** distance is ~3.41 Å) and assembled by $(C{\equiv}N)_2$**Cu(μ-Br)$_2$Cu**$(N{\equiv}C)_2$ rhomboids as secondary building units (SBUs) where each nitrile fragment links different **L**'s. **UDS-6** exhibits several interesting photonic properties such as a large absorption spectrum extending to ~1700 nm, a near-infrared (NIR) and anti-Kasha emission (λ_{em} ~1000 nm), exciton migration across the solid and photoconductivity, all of which drastically differ from those of **L** in the solid state (absorption extends to ~600 nm, λ_{em} ~700 nm, and **L** is not a photoconductor). Density functional theory (DFT) computations indicate that the lowest energy excited states are metal-halide-to-ligand charge transfer (MXLCT) states where the electron rich Cu_2Br_2 units and the electron withdrawing **L** act as the electron density donor and acceptor, respectively. **UDS-6** is a photoconductor on its own and a mechanism study reveals the presence of photo-induced electron transfer (ET) in a 1:1 blend composed of tetraphenylporphyrinzinc(II), ZnTPP, a well-known electron donor, and **L** within the structure of **UDS-6** with a rate, k_{ET}, of 5.4×10^7 s^{-1}, which assigns **L** as the electron acceptor and consequently the charge carrier in **UDS-6**.

1. INTRODUCTION

Rational designs require prior understanding of the properties of both the metallic and organic components to be combined to prepare materials with a targeted property. Such a property could be electric semi- and photoconductivity, a key feature that gives rise to devices such as transistors, sensors, photovoltaic cells, and light-emitting diodes, for examples. In the field of coordination materials, semi- and photo-conducting materials are, in fact, difficult to obtain. Consequently, a careful pre-screening of the organic and inorganic components is required.

In this investigation, the coupling of fluoren-9-ylidene malononitrile (**L**) with a copper halide salt (CuBr) was first assessed based on their physical properties. **L** does not appear as a heavy studied entity throughout the literature but there is enough information to draw a clear picture of its physical properties. Indeed, **L** is prone to intermolecular photo-induced electron transfer,[1,2] where **L** acts as an electron acceptor,[1–3] which has been confirmed theoretically.[4] Concurrently, **L** is found to be electroactive in solution[5] and when used to form a co-polymer with 3,4-ethylenedioxythiophene (EDOT), the resulting materials exhibits a significant electrochemical stability and interesting electrochromic properties.[6] Moreover, **L** is also known to form intermolecular charge transfer (CT) complexes with organic molecules such as bis (ethylenedioxy)dibenzotetrathiafulvalene[7] and *N*,*N*,*N*',*N*'-tetramethyl-*p*-phenylenediamine,[8] which exhibit semi-conductivity properties in the polycrystalline form. Simple structural modifications of this colored dye allow for the formation of insoluble polymers, which can then be used as colorimetric sensors for cyanide ions in water.[9] **L** is also emissive in solution[10] and exhibits a rather short-lived excited state based on flash photolysis absorption spectroscopy (<500 ps).[11] Nitriles are also known to be coordinating entities favouring copper(I), with acetonitrile being a common mono-dentate ligand in some coordination polymers and complexes.[12–14] Therefore, due to its cyano groups, **L** can potentially act as a ligand, but surprisingly, its coordination to transition metals has attracted almost no attention, or turned out simply not possible.[15,16]

Concurrently, the colorless CuBr salt tends to form coordination 0D-complexes and 1D-, 2D- and 3D-polymers with organic ligands, thus demonstrating a significant propensity to form networks and consequently act as an assembling entity. Although statistical data were not accumulated for all donor ligands, a recent survey indicates that the rhomboid motif ($L_2Cu(\mu\text{-}Br)_2CuL_2$) accounts for 72% of all secondary building units (SBUs) built with CuBr, and that among those ~2/3 form

either 1D- or 2D-networks with thioethers for example, with 1D- being less frequent than 2D-coordination polymers, CPs.[17,18] The properties of the $Cu_2Br_2L'_4$ SBU has not been heavily explored, but this white chromophore is often found to be phosphorescent with emission maxima ranging from 370 to 590 nm at room temperature.[17,18] Moreover, photovoltaic cells (with modest power conversion efficiencies, PCEs) were also designed using 1D-coordination polymers of formula $\{Cu_2Br_2[M^{II}L_2](CH_3CN)_2\}_n$ (M^{II} = Cu(II), Ni(II) and L' = cyclic-$[(CH_2)_5N]CS_2^-$) where the electron richer SBU Cu_2Br_2 (Cu(I) and Br^-) and the oxidized metals M(II) act as electron donor and acceptor, respectively.[19,20] These results are fully consistent with that of the analogous semi-conducting 1D-CPs $\{Cu_2I_2[Cu^{II}L'_2](CH_3CN)_2\}_n$ (L' = dithiocarbamate $R_2N\text{-}CS_2$; R = i-Bu, Ph in $R_2N\text{-}CS_2^-$) recently reported.[21] In this investigation, the authors demonstrated that the conductivity takes place through the electron rich Cu_2I_2 SBUs acting as the hole transport entities. Finally, an earlier investigation showed that a thin translucid film composed of a 2D-$(Cu_2I_2(\text{thioacetylene}))_n$ CP (note that the SBU is not a rhomboid in this case, but a 1D-ladder) exhibited a conductivity of 50 Ωcm^{-1}.[22] All in all, despite the scarcity of reported semi- and photoconductivity properties on the rhomboid Cu_2Br_2-containing CPs, one can anticipate that with an appropriate electron acceptor prone to electron transport (i.e. good molecular π-stacking), the design of semi- and photo-conducting materials are readily accessible.

This work reports the rational design of a 2D-CP $[Cu_2Br_2(\mathbf{L})_2]_n$ (**UDS-6**) that is indeed found to be photo-conducting where **L** is demonstrated to act as the electron acceptor and responsible for the charge transport. In addition, this weakly emissive material does not, unexpectedly, follow Kasha's rule, but rather emits from an upper level (S_n; based on spectroscopic findings) in the NIR region. Absence of photosensitization of singlet oxygen, often detectable from its phosphorescence at 1275 nm (7840 cm^{-1}),[23] suggests that the S_1 manifolds are placed indeed below 0.97 eV. Finally consistent with the presence of photoconductivity, a modest exciton migration across the material has also been detected, which is a photophysical process that is useful in solid state photonic devices such as organic light-emitting diodes and photovoltaic cells.

It is noteworthy to mention that the body of literature concerning Cu_2Br_2 (and more broadly CuX) coordination polymers shows mostly UV-absorbing, and Visible-emitting materials with a large Stokes shift, sometimes exhibiting anti-Kasha emission.[17,18,24] All in all, the properties of **UDS-6** are a significant development for the field of CuX coordination polymers.

2. EXPERIMENTAL SECTION

2.1. Synthesis and materials

2.1.1. Materials

All starting reagents and solvents were acquired from Merck, and Sigma-Aldrich and used without further purifications (purity > 95% unless stated otherwise).

2.1.2. Preparation of 2-(9H-Fluoren-9-ylidene)malononitrile (**L**)

To a round-bottom flask containing 95% ethanol (100 mL) were added 9-fluorenone (5 g, 27.7 mmol, 1 eq., CAS-RN 486-25-9), malononitrile (1.83 g, 27.7 mmol, 1 eq., CAS-RN 109-77-3), and ammonium acetate (0.25 g, 3.24 mmol, 0.12 eq., CAS-RN 631-61-8). The mixture was heated to reflux under magnetic stirring for 1h. The yellow suspension acquired a deep orange coloration upon reaction completion. The mixture was brought back to room temperature, then cooled down in the freezer. The product was recuperated by vacuum filtration to afford orange needle-like crystals. Purification was performed by recrystalization from boiling anhydrous ethanol. Yield = 71% (4.52 g). Purity over 99%. This also afforded crystals suitable for SCXRD structure determination. Characterization data was in accordance with literature.[25,26] ^{1}H NMR ($CDCl_3$, 300 MHz) δ (ppm) : 8.36 (d, J = 7.8 Hz, 2H), 7.57-7.46 (m, 4H), 7.31 (td, J_1 = 1.3 Hz, J_2 = 7.6 Hz, 2H). FTIR (cm^{-1}) (Figure S1) : 3077 (w), 2348 (w), 2326 (w), 2223 (m), 2215 (m), 1736 (w), 1720 (w), 1702 (w), 1687 (w), 1655 (w), 1603 (s), 1583 (m), 1563 (s, br), 1445 (s), 1314 (s), 1216 (m), 1176 (s), 1160 (m), 1149 (m), 1111 (s), 1058 (w), 1040 (w), 1009 (w), 978 (w), 948 (m), 904 (m), 873 (m), 784 (s), 723 (s), 691 (s), 665 (s), 630 (m), 616 (w), 576 (w), 513 (m), 465 (m), 424 (m), FT-Raman (cm^{-1}) (Figure S1) : 3076 (w), 3067 (w), 2222 (s), 2214 (s), 1613 (m), 1603 (m), 1583 (m), 1562 (s), 1527 (w), 1372 (m), 1314 (m), 1224 (s), 1215 (s), 1178 (m), 1165 (m), 1110 (m), 1030 (m), 1008 (w), 911 (w), 752 (w), 665 (w), 615 (w), 575 (w), 429 (w), 397 (m), 292 (w), 240 (m), 158 (s).

2.1.3. Preparation of **UDS-6**

Coordination polymer **UDS-6** was prepared by suspending **L** (50 mg, 0.219 mmol, 1 eq.) and copper(I) bromide (63 mg, 0.439 mmol, 2 eq., CAS-RN 7787-70-4) in acetonitrile (5 mL). The

suspension was left undisturbed at room temperature for 16 hours. Black prism crystals suitable for SCXRD were collected from the suspension. For further analyses, these were washed (but not soaked) with acetonitrile (2 x 10 mL) and chloroform (2 x 10 mL). Anal. Calcd for **UDS-6** : C, 51.7; H, 2.17; N, 7.54. Found : C, 50.9; H, 2.10; N, 7.26. FTIR (cm^{-1}) (Figure S1) : 3098 (w), 3060 (w), 3042 (w), 3008 (w), 2345 (w), 2325 (w), 2228 (m), 2214 (m), 1600 (m), 1583 (m), 1540 (s), 1474 (m), 1443 (s), 1310 (s), 1219 (m), 1183 (m), 1169 (m), 1164 (m), 1112 (s), 1007 (m), 990 (m), 944 (w), 872 (m), 787 (s), 723 (s), 661 (s), 566 (m), 512 (w), 458 (w), 444 (w), 425 (m), 389 (s), 351 (s). FT-Raman (cm^{-1}) (Figure S1) : 3064 (w), 2228 (s), 2214 (s), 2171 (w), 1610 (m), 1599 (m), 1581 (m), 1540 (s), 1473 (m), 1374 (m), 1309 (m), 1239 (w), 1218 (s), 1162 (w), 1111 (m), 1028 (w), 1006 (w), 785 (w), 663 (w), 615 (w), 457 (w), 442 (m), 413 (m), 285 (m, br).

2.2. Characterization methods

Solid-state UV-Vis absorbance spectra were acquired on a Varian Cary 300 Bio UV-Vis spectrophotometer equipped with an integration sphere using a reflectance apparatus. Samples were dispersed between two quartz plates.

The solid-state UV-Vis absorbance spectrum of **UDS-6** was measured on a Varian Cary 6000 Bio UV-Vis spectrophotometer in transmission mode corrected to 100% and 0% transmittance baselines. The sample was finely ground, and thinly dispersed between two quartz plates. The measurement of a similarly prepared sample of magnesium sulfate (CAS-RN 7487-88-9) shows that there is negligible influence of diffusion phenomena during measurement (Figure S2).

Solution UV-Vis absorbance spectra were acquired with an HP 8452A diode array spectrophotometer using 1 × 1 cm quartz cuvettes.

Solution and solid-state photoluminescence emission and excitation spectra were acquired either on an Edinburgh Instruments FLS980 or a Horiba PTI QM-400, both equipped with 450W Xe lamps and single-single monochromators. Samples were either dissolved in an appropriate solvent in 1 × 1 cm quartz cuvettes, introduced in a glass capillary, or dispersed between quartz plates. The spectra were corrected for instrument response.

Emission lifetime measurements were performed on an Edinburgh Instruments FLS980 using a microchannel plate PMT and nano-LED lasers (λ = 443 nm; 15 mW; fwhm = 120 ps).

Measurements were performed using the time-correlated single-photon counting (TCSPC) method, and data were treated by multiexponential deconvolution analysis. All values have an uncertainty of 10 % based on multiple measurements.

Emission quenching experiments were conducted by placing a powder dispersion of the donor, acceptor, or blend on quartz plates, and measuring the emission intensity or lifetime according to previously described protocols. Blends were prepared by grinding the powders intimately in a mortar and pestle for 3 minutes.

Temperature-dependent emission spectra were recorded on a Horiba Jobin-Yvon (HJY) Fluorolog-3 (FL3-2iHR550) fluorescence spectrofluorometer equipped with an IR R928P PMT/HJY FL-1073 detector. Low temperature measurements were allowed by using an OptistatCF in the range of 4 K to 300 K sourced from Oxford Instruments. Solid samples were placed in a quartz sample holder inside the cryostat and maintained at the desired temperature until equilibrium was reached before recording the spectrum.

Single crystals of **L**, and **UDS-6** were mounted on a Bruker D8 Venture four-circle diffractometer equipped with an Oxford Cryosystems nitrogen jet stream low-temperature system. X-ray radiation was generated with Mo-Kα radiation (λ = 0.71073 Å) monochromated through graphite from a microfocus IμS tube from Incoatec GmbH. Applying a least-squares fit to the optimized setting angles of the entire set of collected reflections yielded the lattice parameters. Intensity data were recorded as ϕ and ω scans with κ offsets. No significant intensity decay or temperature drift was observed during data collections. SAINT v8.37A software was used to reduce data, and absorption correction was performed using SADABS-2016/2. Structure elucidation was performed using SHELXT with intrinsic phasing. H-atoms were placed geometrically and refined on a riding model. Full-matrix least-squares on F^2 was carried out using SHELXL program on the complete set of reflections. All non-hydrogen atoms were refined with anisotropic displacement parameters, whereas H-atoms were treated in a riding mode.[27–29]

Powder X-ray diffraction patterns were acquired from a small sample of powder dispersed over a ZERO diffraction plate from Charles Supper Company and placed for analysis in a BRUKER D8 ADVANCE diffractometer. Diffractograms were acquired using the DIFFRAC.COMMANDER (version 8.6.3.0) software from BRUKER using Cu Kα (1.54060 Å) as an X-ray source (40.0 kV,

40.0 mA). Data were collected from 4 to 60° (2θ) over 2046 steps (0.027°step^{-1} ; 0.50 s.step^{-1}) using a LynxEye detector. No further data treatment or baselining was done to the acquired diffractograms.

FTIR spectra were recorded on an Agilent Cary 630 FTIR spectrometer using an ATR module, with a resolution of 0.931 cm^{-1}.

FT-Raman spectra were recorded using a Bruker RFS 100/S spectrometer with 1064 nm laser excitation (50-250 mW). The signal was recorded with a photomultiplier Ge-diode, cooled at 77 K. The peak centered around 85 cm^{-1} is an instrumental artefact.

Proton nuclear magnetic resonance (^{1}H NMR) spectra were recorded on a Bruker Advance AS300 NMR spectrometer. Chemical shifts are given in ppm relative to the residual solvent peak.

Elemental analysis (C,H,N) measurements were acquired in triplicate using a Flash 2000 OEA from Thermo Fisher Scientific. The detection limit for nitrogen is 0.05%.

Electrochemical measurements were performed using a BioLogic VMP-300 potentiostat using a glassy-carbon working electrode (d= 3 mm), a platinum wire counter electrode and a silver wire as pseudo-reference electrode in a three-electrode system. Internal standard of 1 mM ferrocene was used to correct the potential recorded. All measurements were performed using water-free solvents degassed with argon using 1 or 2 mM of analyte and 100 mM of tetrabutylammonium hexafluorophosphate (purity = 98%, CAS-RN 3109-63-5) as the supporting electrolyte. Rotating disk electrode measurements were performed using a modulated speed regulator (AFMSRCE) from Pine Research with a glassy carbon rotating disk electrode (d = 5 mm). Kinetic parameter extraction from rotating disk electrode experiment was obtained according to the method presented by Wang et al. to circumvent the slope dependence on potential of the Koutecký-Levich plot present for quasi-reversible systems.[30] The intercept (I_{quasi}) of a Koutecký-Levich plot was determined using linear regression ($R^2 \geq 0.96$) at different overpotentials (η) with E_0' taken to be $E_{1/2}$ obtained at low scan rate in cyclic voltammetry. The obtained I_{quasi}-η curve was linearized and the intercept was obtained through linear regression ($R^2 \geq 0.99$) to extract the heterogeneous standard rate constant (k^0) from the following equation :

$$I_{quasi} = FAk^0C^* \exp\frac{-\alpha F\eta}{RT} \quad (1)$$

Where F is the Faraday constant, A the electrode area, C^* the bulk concentration of the redox specie, α the charge transfer coefficient, R the ideal gas constant, T the temperature.

Photoconductivity and light-dependent cyclic voltammetry measurements were conducted using a Zahner voltammeter from Zennum coupled to a Sciencetech solar simulator (300 nm – 1450 nm AM 1.5). Samples of **UDS-6** and **L** were spincoated (200 µL of a 10 $mg.mL^{-1}$ solution/suspension in $CHCl_3$, 300 rpm) onto fluorine-doped tin oxide (FTO)-coated glass plates as (WE), and dried overnight at 70°C. The prepared samples were brought in contact with aqueous 0.5 M sodium sulfate (purity = 99%, CAS-RN = 7757-82-6) as an electrolyte in a dedicated voltammetry sample holder equipped with a window for irradiation of the sample. A reference electrode (RE) of Ag|AgCl (saturated aqueous KCl), and a platinum counter electrode (CE) were used for all subsequent light-dependent voltammetric measurements. For time-resolved photocurrent measurements, the irradiance was shut on and off at 60 second intervals while a constant potential of ~ +0.05 V was applied.

Excitation-dependent emission spectra were acquired using a variable excitation power laser (SHG from a Solstice Ti-sapphire laser λ = 398 nm; FWHM = 75-100 ps). The detector was a Streak camera (Axis-TRS, Axis Photonique Inc.) with a resolution of less than 8 ps. The results were analyzed by numerically integrating the area under the spectrum curve, and correlating against linear or square-root excitation power.

2.3. Computational methods

All computations were carried out using density functional theory (DFT, ground state) or time-dependent DFT (TDDFT, excited states) with Gaussian 16[31] at the Université de Sherbrooke with the Mammouth supercomputer supported by Calcul Québec and the Alliance de la recherche numérique du Canada. The computational fragments were all adapted from crystallographic coordinates without further optimization. All computations were carried out using the B3LYP functional and the 6-31g basis set for all atoms. The copper and bromide atoms received pseudopotential approximations (GENECP) through the LANL2DZ ECP basis set to avoid the unnecessary computational cost associated with the core electrons. The calculated absorption

spectra were obtained from GaussSum 3.0.[32] Isosurfaces were generated with a contour value of 0.02; red lobes are positive, and green lobes are negative.

3. RESULTS AND DISCUSSION

3.1. Characterization of the ligand in the solid state

During this investigation, **L** was crystalized, and its structure was solved by X-ray diffraction XRD studies. The data are available in the SI (Table S1). A recent report mentioned that two polymorphs of **L** exist : **form 1** ($P\bar{1}$), which has a *head-to-tail* cofacial π-stacking … ABAB…, and **form 2** ($P2_12_12_1$), which has a *head-to-head* π-stacking … AAA…[10] Solid state Raman spectra showed that there is no difference between the two forms. Herein, **form 2** was studied in its solid state with its identity confirmed based on single crystal XRD. However, the reported photophysical data in this recent study reported by Kubendiran and his collaborators[10] turned out to be quite different from those observed herein and needed a revisit since the new findings help the subsequent interpretation. For examples, the authors reported an anti-Kasha emission band at ~450 nm with no new feature beyond 550 nm, and quite ill-defined emission spectra (most likely fluorescence) in the solid state. Figure 1 shows normalized emission spectra of **L** in 2-MeTHF and $CHCl_3$ solutions (left) and in the solid state at 293 K (right). Upon changing the solvent and the relative concentration of **L**, a new emission band clearly associated with aggregations appears at ~650 nm. The excitation spectra super-impose the absorption spectra well in solution (Figure S3) or reasonably well in the solid state (Figure S3, right) indicating that no impurity interferes with the analysis. In the solid state, the low-energy emission band is now placed at λ_{em} = 700 nm and is well-defined and featureless. The emission decay of **L** in 2-MeTHF monitored at 700 nm is mono-phasic with a lifetime of 0.41 ns (Figure S4) attributable to a fluorescence arising from the aggregate (its weak absorption spans from 400 to 550 nm, which is observable upon zooming this region). Upon lowering the temperature, more aggregates are prone to form. Indeed, the emission spectrum of **L** recorded at 77 K in 2-MeTHF exhibits a broad band with a maximum at 548 nm (Figure S5), a shape and position that is indicative of two undeconvoluted bands. The emission decay trace of **L** in 2-MeTHF at 450 nm (*i.e.* the high energy band) can be modeled with a triple exponential, for which the major component has a lifetime of 0.57 ns (Figure S6). Albeit slightly larger, this order of magnitude is consistent to that reported by Estrada *et al*. using flash photolysis

absorption spectroscopy (<500 ps).[11] This short excited state lifetime was attributed to a distortion of the vinylidene double bond C=C(-C≡N)$_2$.[11]

This 450 nm emission is also assigned to fluorescence (non-aggregated). The two other minor components exhibit lifetimes of 7.1 and 3.3 ns but their exact nature cannot be safely assigned, which is not the goal of this analysis. The photophysical parameters are placed in Table 1. Several components of the emission decays are found to be in the μs time scale (Table 1). This analysis indicates that the solid built with π-stacked **L** units will emit towards or in the near-IR region. DFT computations performed on a single **L** molecule, and a tetramer **L**$_4$ using X-ray data were run to obtain (1) the nature of the frontier MOs, and (2) the effects of its π-stacking. First, the atomic contribution of the lone molecule's HOMO (Figure S7) is mainly found to be on the π-fluorene portion of **L** whereas the LUMO exhibits atomic distributions involving all π-orbitals of both moities of the molecule (fluorene and malononitrile). These computational results are fully consistent with those obtained by Diederich *et al.*[4] and those from Estrada *et al.*[11] on **L** and other related molecules bearing malononitrile residues. So, **L** falls into the category of *push-pull* molecules. A HOMO → LUMO transition generates a charge transfer (CT) excited state. Second, upon pilling up four **L** units (atomic positions extracted from the X-ray data), the atomic contribution of the frontier orbitals are not evenly distributed over the four molecules. Instead, the atomic contributions vary significantly from one unit to another (Figure S8) so that a HOMO → LUMO transition leads to an intermolecular CT process added to the intramolecular one. This result may explain the presence of red-shifted features extending all the way to 600 nm (Figure 1, right) instead of 500-550 nm as illustrated by Kubendiran and collaborators.[10]

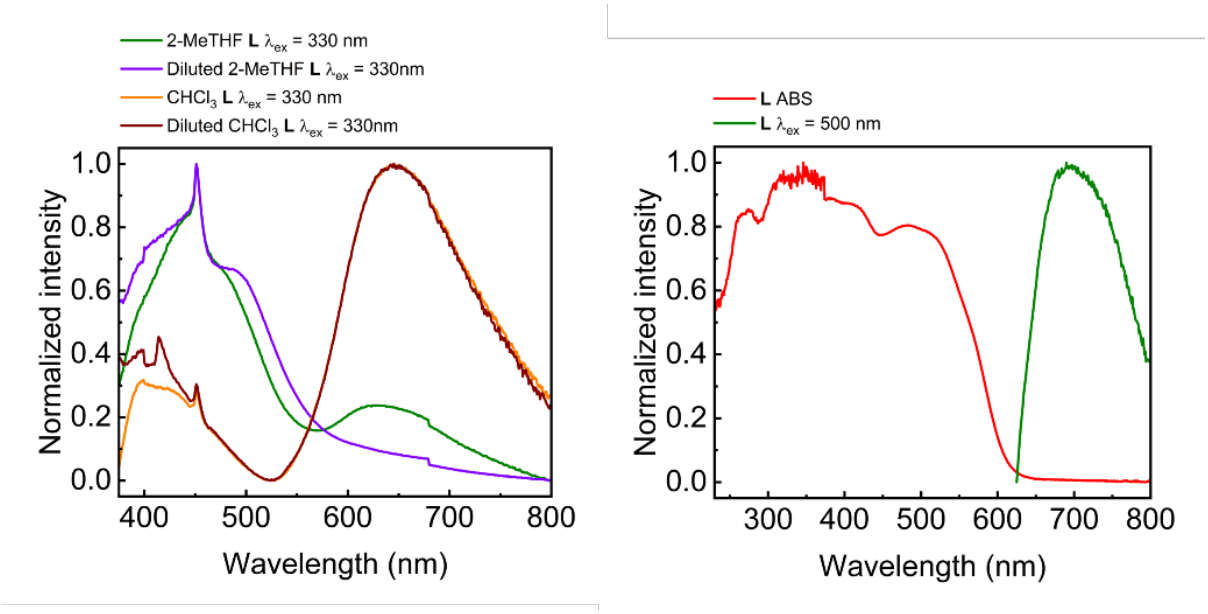

Figure 1. Comparison of the solution (left) and solid-state (right) steady-state spectra of **L**. The spike near 450 nm in the emission spectra in solution is an artefact due to the machine that could not be removed.

Table 1. Photophysical parameters of **L**.

Parameter	293 K solid state	77 K solid state	293 K 2-MeTHF	77 K 2-MeTHF
λ_{abs} (nm)	337, 400, 485	n.d.[a]	438, 349, 266	n.d.[a]
λ_{em} (nm)	– 696	– 692	445 (non-aggregated) 647 (aggregated)	548 (mixture)
τ_{PL} short[b]	0.36 ns (81.7%) 3.8 ns (18.3%)	0.078 µs (8.4%)	0.41 ns (aggregated)	0.77 ns (62.0%)
τ_{PL} long[b]	0.039 µs (17.2%) 1.5 µs (46.5%) 5.2 µs (36.3%)	0.51 µs (24.5%) 2.0 µs (45.6%) 7.3 µs (21.6%)	0.57 ns (non-aggregated) 3.3 ns (non-aggregated) 7.1 ns (non-aggregated)	2.9 ns (7.55%) 15 ns (30.5%)
Φ_{PL}	<0.01	n.d.[a]	n.d.[a]	n.d.[a]

[a] n.d. : not determined. [b] Emission lifetimes satisfying the equation $I(t) = \sum_i B_i \exp(-t/\tau_i)$ with percent contributions satisfying equation $f_i = \tau_i B_i / \sum_j \tau_j B_j$. All decays are placed in the SI (Figures S4, S6, S9-12).

3.2. Synthesis and X-ray diffraction of UDS-6

UDS-6 was obtained upon reacting **L** with CuBr in acetonitrile and black crystals suitable for single X-ray diffraction (SCXRD) were obtained from the suspension (Scheme 1, Table S1). The structure reveals a 2D-CP of formula $[Cu_2Br_2\mathbf{L}_2]_n$ where the SBU is the rhomboid Cu_2Br_2 unit (Figure 2a). The coordination environment of the Cu_2Br_2 rhomboid is constituted of four distinct **L** molecules, which then propagate the network. Each layer is built on *head-to-tail* dimers, $\mathbf{L}_2$, thus creating a "double layer" effect for a single sheet of **UDS-6** (Figure 2b). The graphite-like construction completes the overall structure (Figure 2c,d).

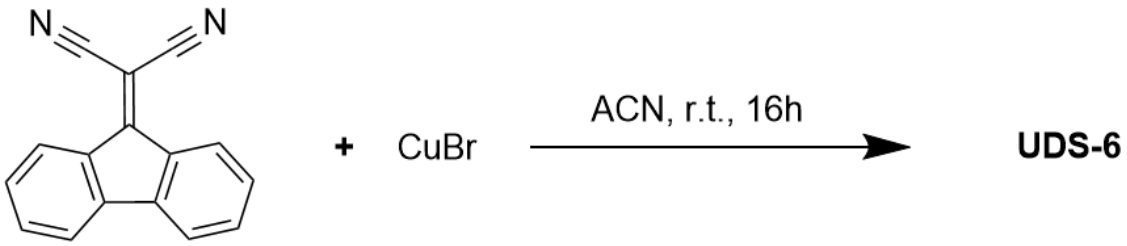

Scheme 1. Reaction between **L** and CuBr to form **UDS-6**.

The Cu···Cu distance of the $(CuX)_n$ unit (X = Cl, Br, I; n = 1, 2, 3, 4, …) is often viewed as a key parameter that defines the photophysical properties arising from the SBUs. For the Cu_2Br_2 rhomboid, when the Cu···Cu separations approaches or is less than the sum of the van der Waals radii (2.80 Å), often driven by the medium rigidity, then this SBU has a strong tendency to be emissive.[17,18] Otherwise, this motif is rather optically silent. The Cu···Cu separation in **UDS-6** is found to be 3.15 Å, and therefore the cuprophilic interactions are minimal (if any).[18] The outcome is that no low-energy cluster-centered excited state (^{3}CC) is formed.[18,24]

The minimal distance between the 2D-layers is found to be 3.55 Å based on the intermolecular separation between the π-systems of the coordinated **L** molecules, which is longer than that of the interplanar distance between two C-sheets in graphite. This difference stems from two contributions. First, the presence of bromides slightly sticking out of the layer's surface (ionic radius of Br^- is 1.96 Å). Second, there are two crytallographycally different sets of $\mathbf{L}_2$ dimers and the angle made by their respective average planes is 7.28°, which makes some C-atoms sticking out the surface as well. Concurrently, the interplanar **L**···**L** distance within the 2D-network is ~3.42

Å, indicating that the Cu_2Br_2 SBUs assembled the cofacial *head-to-tail* dimers in a weak interaction fashion. Consequently, there is a need to monitor the π-stacking effect. This phenomenon is already perceptible in the π-stacked $\mathbf{L}_4$ presented in Figure S8 stressing the dissymmetry of the atomic distributions on each **L** in the frontier MOs. Recent examples include cofacial bis(aromatic)s such as in paracyclophanes[33,34] and bis(porphyrin)s.[35,36]

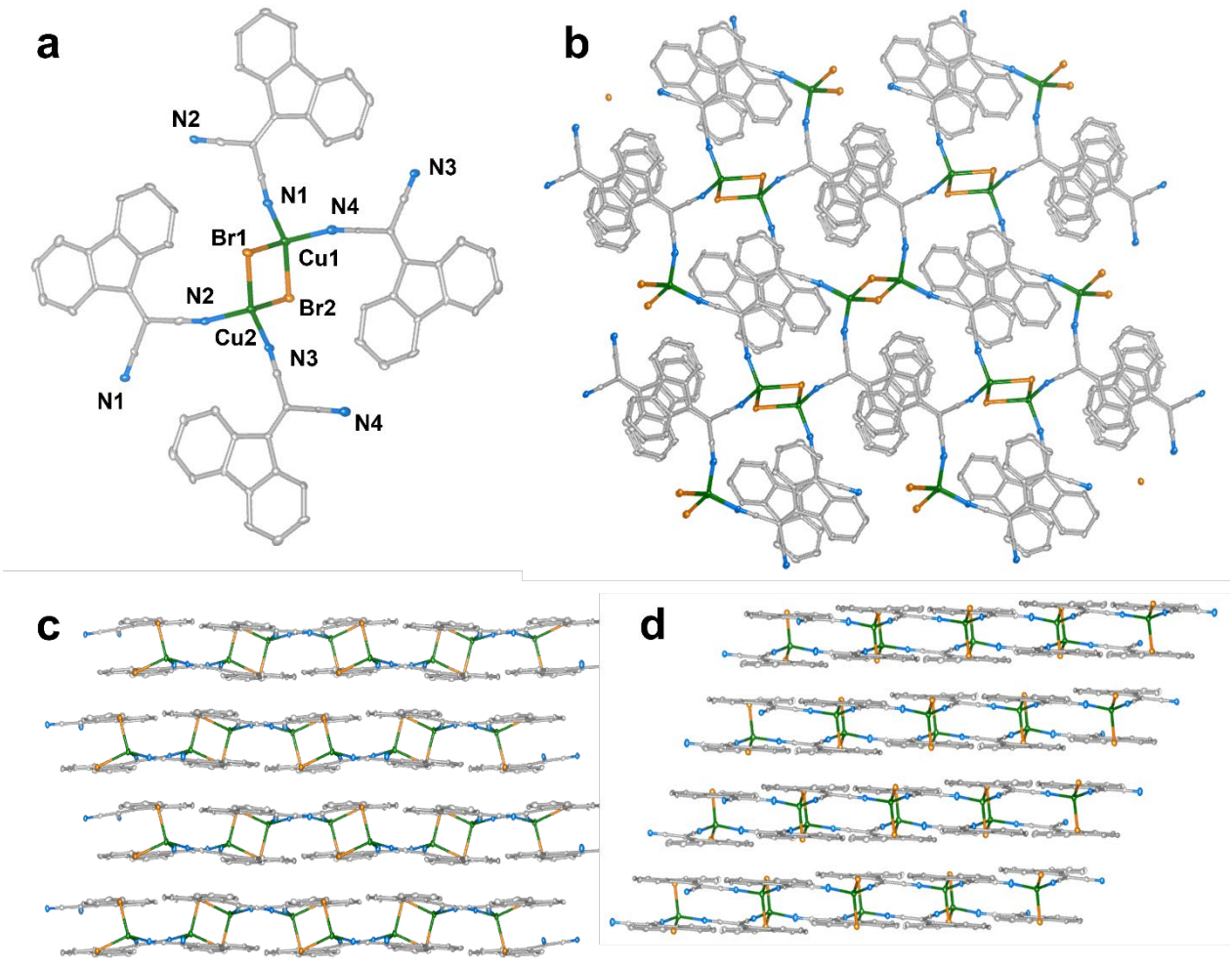

Figure 2. Crystal structure of **UDS-6**. (a) Coordination environment of the Cu_2Br_2 rhomboid. (b) Top view showing the 2-dimensionality. (c) Packing of the double layers seen through the a unit cell axis. (d) Packing of the double layers seen through the b unit cell axis. Rendered using VESTA freeware.[37] Gray : carbon, blue : nitrogen, green : copper, orange : bromine. The thermal displacement ellipsoids are drawn at 50% probability. Cu1-Cu2 = 3.1507(13) Å, Cu1-N1 =

1.964(7) Å, Cu1-N4 = 2.001(7) Å, Cu1-Br1 = 2.4521(13) Å, Cu1-Br2 = 2.5207(12) Å, Cu2-Br1 = 2.4848(12) Å, Cu2-Br = 2.4820(12) Å, Cu2-N2 = 2.010(7) Å, Cu2-N3 = 1.966(7) Å.

The powder diffraction (PXRD) of **UDS-6** in its polycrystalline form compares favorably to that of the calculated one issued from the X-ray data of the crystal structure Figure 3 exhibits this good comparison and confirms the identity and purity of the powder used for the subsequent analysis. While the relative intensities of some peaks differ from the simulated pattern, this is to be expected in real samples where some planes are preferred, and others (here, along the 2D sheets) more easily cleaved. In addition, the relatively straight baseline is indicative that the contribution of amorphous domains is readily minimal.

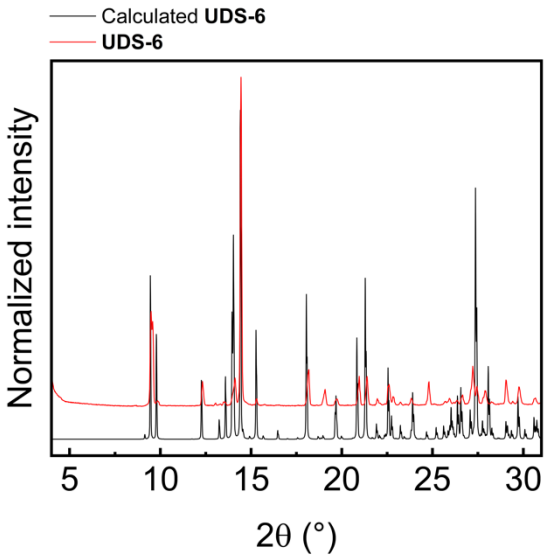

Figure 3. Powder X-ray diffraction pattern of **UDS-6** compared to the calculated data. The full diffractogram is given in Figure S13.

The comparison of the nitrile's region of the FTIR and FT-Raman spectra of **L** and **UDS-6** shows a considerable shift in the frequency associated with these modes (*vide supra*), and confirms the coordinating action of the nitrile, despite the weak coordination bond it is known to make.

3.3 Photophysical characterization of UDS-6

The absorbance spectra indicate that the black **UDS-6** powder does indeed absorb the entire visible spectrum, with some absorption also in the UV and NIR regions of the spectrum (Figure 4).

Compared to the solid-state spectrum of **L** (Figure 1, left), the additional long absorption tail extending all the way to ~1700 nm, is readily depicted. At first glance, the assignment for this feature appears to be metal-halide-to-ligand CT (MXLCT) since the only significant difference between **L** and **UDS-6** is the addition of the electron rich Cu_2Br_2.

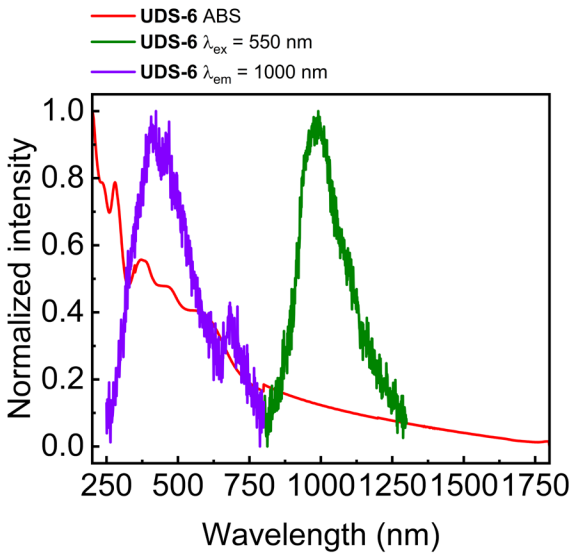

Figure 4. Steady-state absorbance at 293 K (red), excitation (purple), and emission (green) spectra at 293 K of **UDS-6** (wavelength axis depicted here, and wavenumber axis depicted in Figure S14). Note that no baseline correction was necessary as the comparison with powdered $MgSO_4$ as baseline was straight (Figure S2) and that the correction factor becomes inadequate below 300 nm.

To address the nature of the low-lying excited states, DFT computations were performed. For this, the model [Cu_2Br_2**L**$_4$] (Figure 5) was employed from X-ray data. The HOMO exhibits a major series of atomic contributions centered onto the Cu_2Br_2 SBU, with some minor contributions onto the four π-C≡N linkages. The LUMO exhibits atomic contributions spread all over one **L** π*-system, with modest contributions of the adjacent copper atom and another malononitrile unit. While the localization of the MOs is given with sufficient reliability, the calculated MO energies must be taken with caution because this model is incomplete and lacks sufficient electron rich Cu_2Br_2 units, a situation associated with the limited size of computations and the nature of polymeric and solid state compounds.[38,39] Nevertheless, the HOMO → LUMO transition leads to the formation of a metal-halide-to-ligand charge transfer (MXLCT) excited state. This outcome is

consistent with analogous rhomboid-containing complexes for which computations also indicated the presence of lowest-energy excited states of the type MXLCT where M = Ag(I), and L = C≡N.[40] Despite the inconvenience, TDDFT was employed to assess the relative intensity of the low-energy electronic transition (all the data are placed in Table S2, Figure S15-S16). The calculated lowest energy transition is found at 1052 nm with an oscillator strength of 0.0237 and molar extinction coefficient of 13 000 $M^{-1}cm^{-1}$, which indicates a good absorptivity.

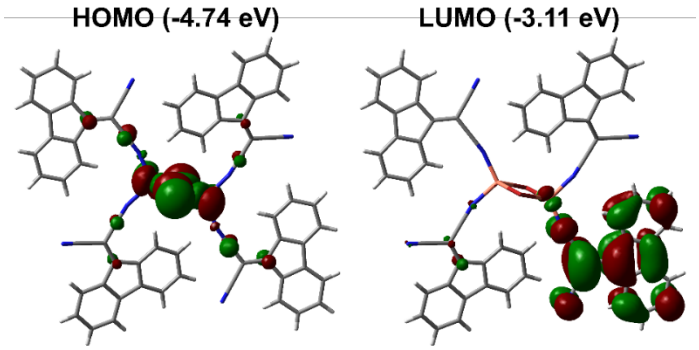

Figure 5. Representation of the frontier molecular orbitals of a $Cu_2Br_2\mathbf{L}_4$ cluster from **UDS-6**.

It is noteworthy that a weak emission band at λ_{em} ~1000 nm of this 2D-CP is observed (Figure 4). The excitation spectrum superposes well the absorption one and confirms its identity. Moreover, this ~1000 nm band turns out to be extremely red shifted in comparison with other rhomboid $Cu_2X_2L_4$-based CPs. Indeed, in most M_2X_2-rhomboid-containing (M = Cu(I), Ag(I); X = Cl^-, Br^-, I^-) coordination materials, the expected luminescence is in the 370 to 590 nm region at room temperature.[17,18] This outcome is due (a) to very weak cuprophilic (or argentophilic if M = Ag(I)) interactions limiting the predominance of ^{3}CC emission over the ^{3}MXLCT emission, and (b) to the use of ligands exhibiting high-energy π*-systems (pyridines, phosphines, thioethers, thiones, etc.) However, for the highly colored chromophore **L**, the energy gap between the π- and π*-manifolds is smaller, and consequently this feature also reflects on the energy gap between the ground and MXLCT excited state in **UDS-6**. Moreover, this emission (λ_{em} ~1000 nm) is placed at higher energy than the lowest-energy absorption tail starting near 1700 nm, an anti-Kasha behaviour that is curiously reminiscent to that of **L** (see comments above) is deduced.[24] In order to assign the anti-Kasha emission, the emission decays were recorded at 800 nm as the limit of the TCSPC detector stops being sensitive towards this area. The photophysical data are summarized in Table 2. The

emission lifetimes are found to be in the ns time scale. Considering that the Cu_2Br_2 induces a heavy atom effect on the photophysical processes occurring at the singlet states (i.e. significant spin-orbit coupling thus increasing the intersystem crossing rate constant), then these excited states are expected to undergo faster depopulation. By comparison with the data for **L** in the solid state, the decrease of the longer components from μs in **L** (Table 1) to ns and long-ns in **UDS-6** (Table 2), perfectly reflects this effect. Consequently, this emission can be assigned to a fluorescence. Moreover, the low intensity of this fluorescence band can be attributed to three basic phenomena; (1) singlet excited state depopulation by heavy atom effect, which affect both lifetimes and quantum yields, (2) re-absorption of the emitted light in the 800-1500 nm range by the solid also absorbing in this same region, and (3) possibility of additional relaxation processes of this emitting excited state (i.e. internal conversion and intersystem crossing). This anti-Kasha fluorescence is unusual compared to a classic case of azulene, where a large gap between the upper singlet excited state S_2 and the lower on, S_1, exists. This large gap permits depopulation of S_2 going straight to the ground state while emitting a photon, S_0, by-passing S_1. In **UDS-6**, this is not a unique case of such phenomena. Other similar but rare examples of metal-containing polymers exhibiting non-Kasha emission occurring in a "crowded" region of excited states and absorption bands have been reported.[41,42] Concurrently, no emission signal associated with the phosphorescence of single oxygen, $^1O_2(g)$ (λ_{em} = 1275 nm; 7840 cm^{-1}), was detected at the solid state/air interface indicating that either the quantum yield of photosensitization is inefficient, or the lowest energy triplet excited state, T_1, of **UDS-6** is not energetic enough for energy transfer. This latter hypothesis is consistent with the fact that the absorption spectrum extends all the way to ~1700 nm (~ 5900 cm^{-1}), a quantity of energy too small for the photosensitization of $^1O_2(g)$.

Table 2. Photophysical parameters of **UDS-6**.

Parameter	293 K solid state	77 K solid state
λ_{abs} (nm)	280, 377, 451, 570, 1000-1700 (tail)	n.d.[a]
λ_{em} (nm)	991	986
τ_{PL}[b]	*0.08 ns (2%)*[c] 3.8 ns (3%) 10.8 ns (34%) 22.2 ns (61%)	n.d.[d] 0.16 μs (34%) 2.7 μs (66%) n.d.[e]
Φ_{PL}	<0.01	n.d.[a]

[a] n.d. : not determined. [b] Emission lifetimes satisfying the equation $I(t) = \sum_i B_i \exp(-t/\tau_i)$ with percent contributions satisfying equation $f_i = \tau_i B_i / \sum_j \tau_j B_j$. All decays are placed in the SI (Figure S17-S18). [c] With a lifetime under the IRF of the laser (~150 ps), this component cannot be expressed with accuracy. [d] a shorter ps-component could be observed but could not be evaluated. [e] a longer component (probably µs) can be seen but could not be measured due to its very low intensity.

Aiming at observing other emission bands, notably phosphorescence, the temperature-dependent emission spectra of **UDS-6** were also measured between 4 and 300 K. No new feature appeared in the 800-1300 nm spectral window and no considerable shift of the ~1000 nm band occurred (Figure 6). The full-width at half maximum (FWHM) also remained relatively constant indicating that no new features appeared under this envelope.

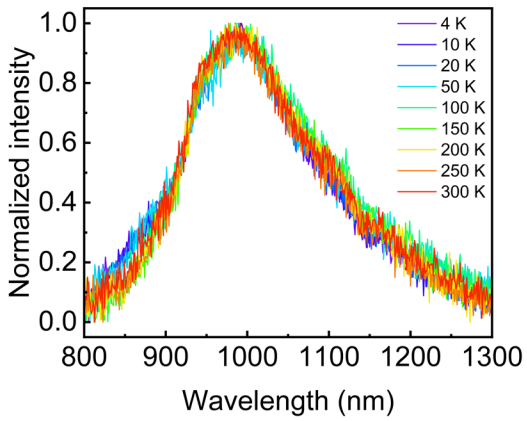

Figure 6. Steady-state luminescence spectra of **UDS-6** as a function of temperature.

Exciton migration or excitation energy migration across a solid is an important photophysical event that finds important implications for photonic devices. This process is common for organic materials but is extremely rare for coordination materials. Incidentally among the scarce examples, one conveniently finds the rhomboid-containing CPs : $[Cu_2X_2\{\mu\text{-EtS}(CH_2)_4SEt\}_2]_n$ where X = Cl, Br, I.[43,44] One detection method consists at the second-order process assessing singlet-singlet (or triplet-triplet) annihilation event (M = molecule); 2 $M(S_0)$ + 2hν → $M(S_1)$ + $M(S_1)$ → $M(S_0)$ + $M(S_n)$ (n > 1) + heat; $M(S_n)$ → $M(S_1)$ + heat; $M(S_1)$ → $M(S_0)$ + hν' (note that for triplet states, these equations are the same except that S_x is replaced by T_x). The generation of a high number of

excitons, $M(S_1)$, is performed using a high intensity source (commonly a laser) and as the number of excitons increases, singlet-singlet annihilation ($M(S_1) + M(S_1) \rightarrow M(S_0) + M(S_n)$ ($n > 1$) + heat) occurs more frequently. Consequently, a graph of emission intensity (I_F) *vs* laser power (i.e. photon flux) will not follow a linear relationship, but rather will follow a linear relationship when the x-axis is (laser power)$^{1/2}$. This process turned out possible when the chromophores are placed close enough to each other, something that thioethers can do through a short Cu-S-Cu bridge in these three (X = Cl, Br, I) earlier examples : $[Cu_2X_2\{\mu\text{-}EtS(CH_2)_4SEt\}_2]_n$. For **UDS-6**, both graphs are represented in Figure 7ab, but neither exhibits a linear relationship. Instead, a linear portion is depicted at low power in graph I_F *vs* laser power, and then as the power increases, I_F deviates from linearity downward indicating loss of light energy. Similarly, a clear linear portion with a negative intercept of the I_F data at high laser power in the graph I_F *vs* (laser power)$^{1/2}$ is shown, but also exhibits a slight curve at low laser power. This behaviour indicates that a low power, no obvious annihilation takes place, but as the 2D-CP becomes *saturated* in the number of excitons, then annihilation occurs more visibly. The measurements of the fluorescence lifetimes *vs* laser power (limited to two components for simplicity), exhibit a decrease of the longest-lived component as the power increases, thus witnessing quenching by singlet-singlet annihilation (Figure 7cd). The short component does not appear sensitive to the laser power, thus indicating absence of annihilation and therefore of exciton migration. This duality suggests the presence of two sites; one promotes exciton migration, and one does not. It is noteworthy that for a lifetime of ~10 ps, the rate of unimolecular excited state deactivation is $10^{11,}$ which is ultrafast. So, if the quenching rate is 10^8 to 10^9 s^{-1}, like for the longer component, the quenching by singlet-singlet annihilation is unlikely.

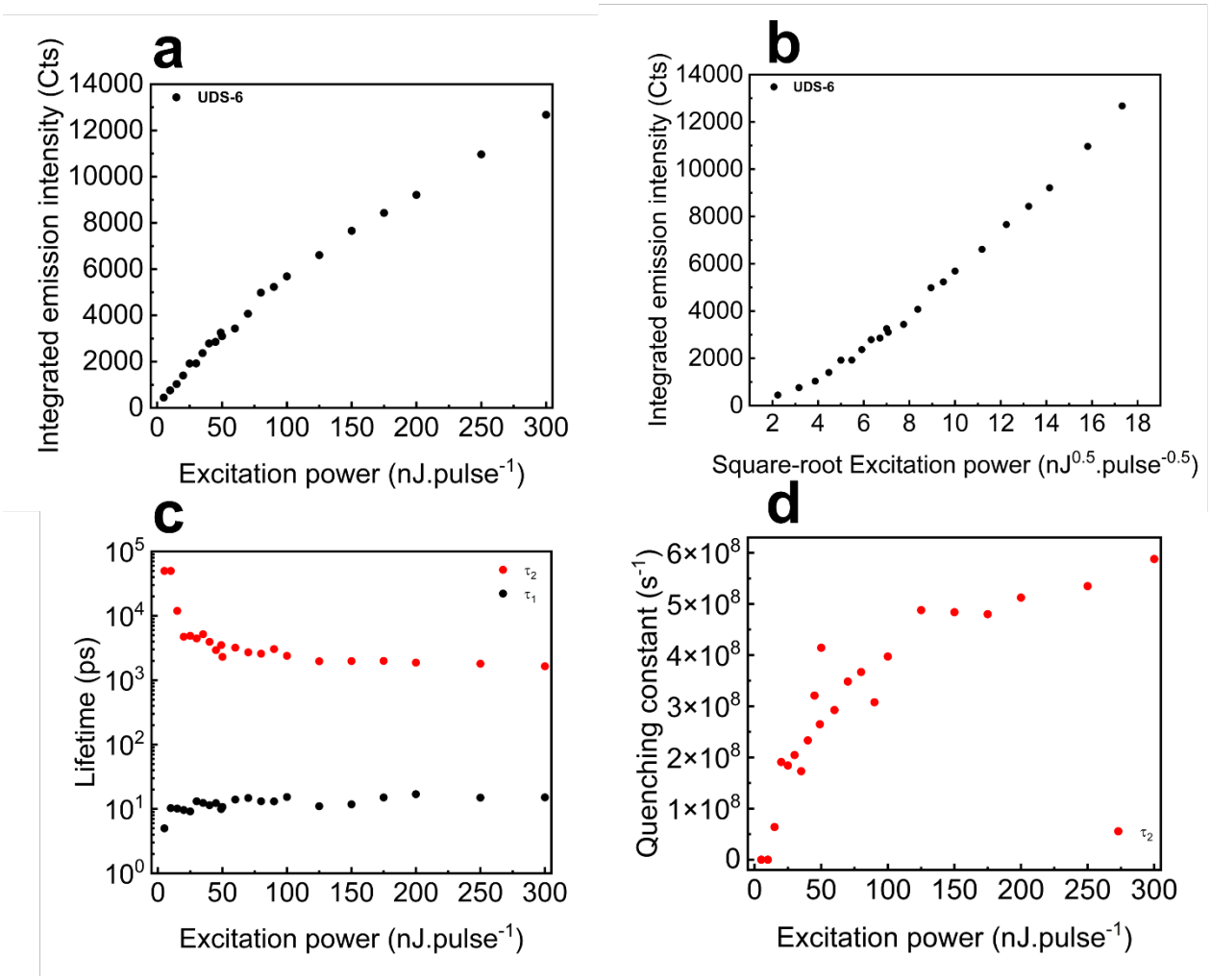

Figure 7. emission intensity (area under curve) as a function of laser power, (a) linear power axis on the left and (b) square-root power axis on the right. (c) Fluorescence lifetimes of **UDS-6** as a function of laser power. (d) Quenching rate $k_q = \frac{1}{\tau} - \frac{1}{\tau_0}$ for the longest-lived component, where τ is the emission lifetime at a given power, and τ_0 is the unquenched emission lifetime.

Within the 2D-layer, the Br^-•••Br^- separations are ~8.78, ~10.31, and ~11.12 Å. Between two layers, the closest Br^-•••Br^- distance is ~5.83 Å. However, two slightly different packings of **L** in the crystal structure of **UDS-6** were observed. These interplanar **L**•••**L** distances within a 2D-layer are either 3.36 or 3.31 Å depending on the pathway and are 3.45 or 2.86 depending on the pathway between 2D-layers (respectively). As the rate for energy transfer is strongly dependent on the donor-acceptor separation ($k_{EnT} \propto r^{-6}$),[45] the existence of two different pathways for energy

migration between several 2D-layers through interplanar **L•••L** separations (A = 3.36 + 3.45 +3.36 + 3.45 + … Å ; B = 3.31 + 2.86 + 3.31 + 2.86 + … Å, Figure 8) may very well explain the saturation.

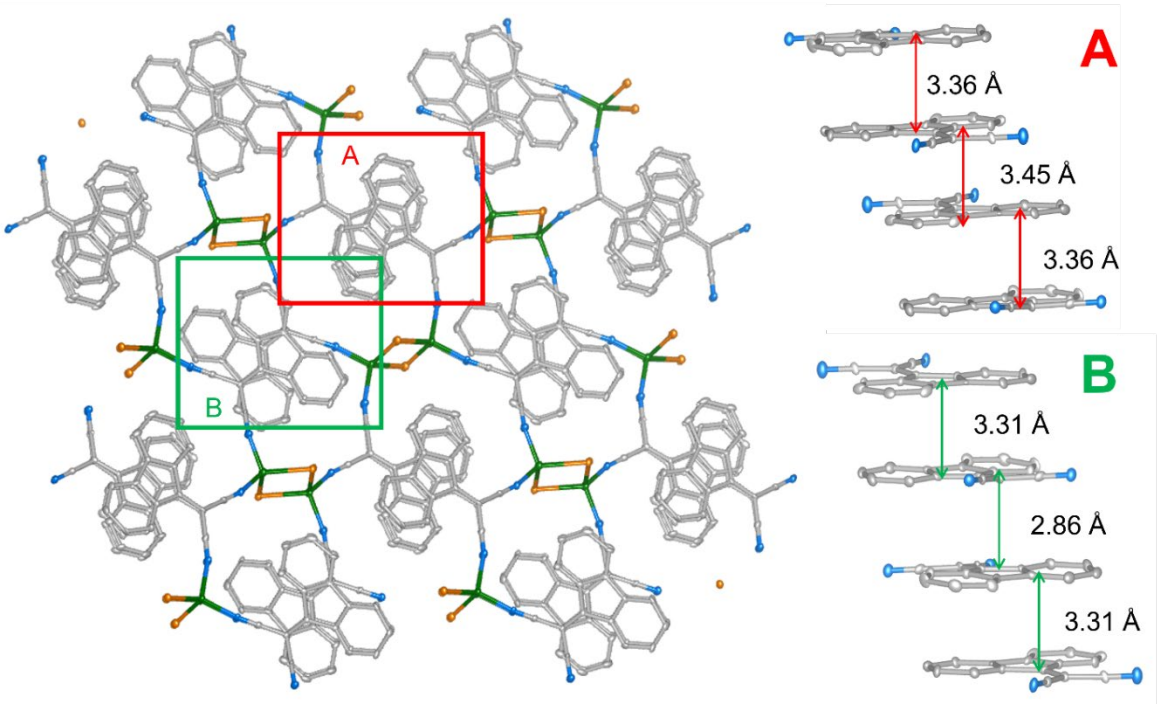

Figure 8. Representation of different possible exciton migration pathways in **UDS-6**.

Indeed, as the medium of **UDS-6** is posited to be identical in nature across the material, the only variable on which the rate of energy transfer only depend is the term κ^2/r^6, where κ^2 is an orientation factor which is equal to ~4 when the transition moments are parallel, which is the case for all crossings in both pathways here, and r is the interchromophoric distance. This gives the parameters present in Table 3, showing a clear preference for pathway B. In any event, the global difference is quite small, and the rather small (10^8 s^{-1}) quenching constant points to rather slow singlet-singlet annihilation and energy migration processes.

Table 3. Interchromophoric distances and relative exciton migration parameters for both pathways. The faster processes belong to the B pathway, with a limiting process being in the intra-layer **L•••L** crossing. Nevertheless, these processes are rather similar, and would be expected to competitively occur.

L•••L Crossing	**Pathway A**		**Pathway B**	
	r (Å)	**κ^2/r^6 (x 10^{-3} Å^{-6})**	**r (Å)**	**κ^2/r^6 (x 10^{-3} Å^{-6})**
Intra-layer	3.36	2.80	3.31	3.04
Inter-layer	3.45	2.39	2.86	7.28

3.4. Ligand-mediated photo-induced electron transfer

The use of a electron-rich node, and of an electron-poor ligand may induce charge separation, which can be in turn used for photovoltaic applications. Due to this fact, copper(I) halide rhomboids, commonly perceived as electron rich moieties, linked to electron acceptor ligands have been previously assessed as sensitizers in dye-sensitized solar cells (DSSCs).[19–22] The reported PCEs were found to be rather modest. Furthermore, visible-absorbing photoelectroactive materials have been explored in literature as components in organic photovoltaics (OPVs), but literature shows no example of a CuX coordination material used in this way. To probe **UDS-6**'s photo-electrochemistry, a photoluminescence quenching experiment was performed using fullerene $PC_{71}BM$ (CAS-RN 609771-63-3), a well-known electron acceptor, and **UDS-6** as a potential electron donor. However, **UDS-6** did not quench the fluorescence of $PC_{71}BM$ ($PC_{71}BM^{-\bullet}$ is non emissive; Figure S19), signifying that the MO energies of **UDS-6** are not placed appropriately to donate electrons to $PC_{71}bm$ and other common OPV acceptors having similar MO energies. This concurs with the MO energies computed above, these being too high for any overlap to exist in the wavefunction potential curves of the D*+A and $D^{+\bullet}$+$A^{-\bullet}$. Concurrently, the same experiment using the well-known electron donor ZnTPP (CAS-RN 14074-80-7), and **UDS-6** as a potential electron acceptor, was performed. It is noteworthy that recent studies based on the Stern-Volmer approach showed that porphyrin derivatives in solution act as electron donors while **L** acts as an electron acceptor upon visible light irradiation.[1,2] In this work, a pronounced quenching of both fluorescence intensities, *i.e.* solid ZnTPP and **UDS-6** (1:1 solid powder blend), was observed (Figure S20). The

fluorescence quenching was also accompanied by a decrease in fluorescence lifetimes (Table 4, Figures S21-S23). Using the following relation, the quenching rates, k_q, were evaluated:

$$k_q = \frac{1}{\tau_D} - \frac{1}{\tau_D^0} \quad (2)$$

where τ_D and τ_D^0 are the emission lifetimes of the energy or electron donor in the presence and the absence of the acceptor. The efficiency of quenching in percent, η, is given by k_q/τ^{-1}. The resulting kinetic data are placed in Table 4 and the emission decays are found to be multi-exponential. To assess the relative quenching rate, the first component of the pristine sample was compared to that of the blend, the second one with the second, and so on, thus allowing for a qualitative comparison of the orders of magnitude of k_q. Because both sets of fluorescence lifetimes decrease, then both photo-oxidative and photo-reductive electron transfer processes occur simultaneously (^{1}ZnTPP* + **UDS-6** → ZnTPP$^{+\bullet}$ + **UDS-6**$^{-\bullet}$ and ZnTPP + ^{1}**UDS-6*** → ZnTPP$^{+\bullet}$ + **UDS-6**$^{-\bullet}$; the radical species are non-emissive). Such photophysical behaviour is reminiscent to that of nonfullerene electron acceptors (NFAs), since the MO energies of ZnTPP and **UDS-6** are appropriately placed, electron transfer occurs with **UDS-6** as an acceptor. The k_q values listed in Table 4 span from 0.6 x 10^8 to 9.8 x 10^9 s^{-1}, which are not considered ultrafast, particularly when the photo-processes occur in the solid state. Similarly, quenching efficiencies ranging from ~50 to 70 % for ZnTPP, and from 60 to 85 % for **UDS-6**, are rather considered medium, again for solid state. Finally, ^{1}ZnTPP* may also be deactivated by singlet-singlet energy transfer: ^{1}ZnTPP* + **UDS-6** → ZnTPP + ^{1}**UDS-6***, as a concomitant competitive process. This process contributes to the overall quenching rate ($k_q = k_{ET} + k_{EnT}$, where ET = electron transfer, and EnT = energy transfer). This is particularly true when the fluorescence band of ZnTPP overlaps entirely with the absorption envelope of **UDS-6** (*i.e.* which leads to a large value of the *J*-integral of the Förster theory).[45] The evaluation of k_{ET} (^{1}ZnTPP* + **UDS-6** → ZnTPP$^{+\bullet}$ + **UDS-6**$^{-\bullet}$) and k_{EnT} (^{1}ZnTPP* + **UDS-6** → ZnTPP + ^{1}**UDS-6***) requires the use of femtosecond absorption spectroscopy (fs-TAS), which cannot be applied to powders. Since the photoelectronic behaviour of **UDS-6** is similar to that reported for **L**, and the localization of the material's LUMO on the **L** fragment, it can be said that **UDS-6** acts as an electron acceptor, through **L**.

Table 4. Fluorescence lifetime and k_q data of ZnTPP and **UDS-6** in the solid state at 293 K.

ZnTPP			
τ^0 pristine (f %)	τ blend (1:1) (f %)	k_q (s^{-1})	η
0.232 ns (15 %)	0.071 ns (25 %)	9.8 x 10^9	70 %
0.586 ns (44 %)	0.24 ns (52 %)	2.4 x 10^9	58 %
1.345 ns (41 %)	0.70 ns (24 %)	0.7 x 10^9	49 %
UDS-6			
τ^0 pristine (f %)	τ blend (1:1) (f %)	k_q (s^{-1})[b]	η
0.080 ns *(1.9 %)*[a]	0.16 ns (25 %)		
3.81 ns (3.0 %)	0.58 ns (19 %)	15 x 10^8	85 %
10.8 ns (34.6 %)	2.33 ns (16 %)	3.4 x 10^8	78 %
22.2 ns (60.6%)	9.35 ns (39 %)	0.6 x 10^8	60 %

[a] With a lifetime under the IRF (150 ps), this value cannot be considered precise. [b] Here $k_q = k_{ET}$.

Seeing this behaviour unfolding in the rather polar medium of **UDS-6** (arising from the cohabitation with metal halide CuBr nodes), a study of its electrochemical behaviour was conducted. To investigate the potential phenomena that can be controlled when designing future coordination materials involving the **L** fragment as a ligand, its heterogeneous electron transfer rate (k^0), LUMO positions and the associated half-wave potential ($E_{1/2}$) were measured in different solvent environments (dry and degassed acetonitrile (ACN), tetrahydrofuran (THF), and methylene chloride (DCM)). Cyclic voltammetry experiments first were performed to obtain LUMO energy levels from the $E_{1/2}$ (Table 5, Figures S24-26).[46]

Table 5. Half-wave potentials, and heterogeneous standard rate constant of **L** in different solvents.

Solvent	**$E_{1/2}$ (V vs. Fc/Fc^+)**	**LUMO (eV)[a]**	**k_0 (10^{-3} cm.s^{-1})**
ACN	-1.07	-4.03	24.9
THF	-1.21	-3.89	4.73
DCM	-1.14	-3.96	2.45

[a] Determined from the half-wave reduction potential, and the HOMO value of Fc (-4.8 eV).

These values remained relatively unchanged as a function of solvent, and hints at the fact that the polarization environment likely has little effect on the LUMO of the **L** molecule. However, the measured LUMO of **L** is rather different to the computed LUMO of the fragment Cu_2Br_2**L**$_4$ used to represent **UDS-6** (-3.11 eV) suggesting that there is a significant interaction between the Cu2Br2

node and the ligand, with a certain degree of electronic wavefunction mixing between both fragments, creating a new entity. This is typical of coordination polymers. Nevertheless, some tendencies in the ligand, such as electron accepting behaviour, can be extracted due to the LUMO of **UDS-6** being located on **L** units. Given that the oxidation and reduction potentials exhibited scan rate dependent variation characteristic of an electrochemical quasi-reversible system, rotating disk electrodes (RDE) were then used to perform Koutecký-Levich analyses as described by Wang et al.[30,47] The quasi-reversible current (intercept of Koutecký-Levich plot) was obtained at different over-potentials in order to assess k^0 in the aforementioned solvents (Table 5, Figure S27).[30,47] For solvents of similar polarity like DCM and THF, similar heterogeneous electron transfer rate were obtained. However, in a more polar solvent like ACN electron transfer rate was significantly increased. Seeing that there is a drastic variation in heterogeneous electron transfer rate according to the polarization environment, it can be assumed that there is a variation in reorganizational energy (Eq. 3), nuclear frequency factor, and/or electronic transmission coefficient.[48] It is proposed that the drastic change observed cannot solely be related to the two latter phenomena because such factors should be similar for the same electrode surface and the same redox species. Therefore, the change in heterogeneous electron transfer rate is attributed mainly to the change in the reorganizational energy λ.[49]

The Marcus theory for electron transfer is :

$$k_{ET} = A \exp\left(-\frac{(\lambda+\Delta G^0)^2}{4\lambda k_B T}\right) \quad (3)$$

where A is an arbitrary pre-exponential factor, λ is the reorganization energy, ΔG^0 is the Gibbs free energy, k_B is the Boltzmann constant, and T is the absolute temperature.[49]

Some parallels can be made regarding the parameters ΔG^0 and λ, which hints at the possible modulation of the PET process through structural tuning. It is envisioned that structures with more or less rigidity, regional polarity, etc. will affect this parameter λ consequentially, and lead to different performances in PET, and, eventually, photocurrent generation.

3.5. Photoconductivity and SBU contribution to hole transport.

Moreover, as for several photo-induced electron transferable materials, **UDS-6** was found to generate a photocurrent upon simulated solar irradiation (Figure 9).[19–22] It is notable that this photocurrent density is ~12.6 $nAcm^{-2}$ compared to the null photocurrent found in **L** when prepared in the same conditions. This result indicates that there are obvious contributions of both the Cu_2Br_2 SBU and **L** (as charge carrier) to the photoconductivity. If the **L** fragments act as the obvious charge carriers due to their role in accepting electron transfers, and their role in the MXLCT transition, its hole-carrying counterpart would obviously be the Cu_2Br_2 polynuclear entities. The conclusion that the Cu_2Br_2 center acts as a hole carrier is consistent with the fact that its iodide homologue, the rhomboid Cu_2I_2 SBU, acts as a hole transport entity.[21] Since mostly visible and NIR light is used to promote conductivity, then the mechanism for the photoconductivity in **UDS-6** is most likely : $[Cu_2Br_2] + {}^1[\mathbf{L}]^* \rightarrow [Cu_2Br_2]^{+\bullet} + [\mathbf{L}]^{-\bullet}$ since the LUMO is located in the π*-system of **L** (Figure 5). Thus the hole and charge transports should occur through the $[Cu_2Br_2]^{+\bullet}/[Cu_2Br_2]$ and $[\mathbf{L}]^{-\bullet}/[\mathbf{L}]$ layers, respectively.

It is remarkable that some negative current density flows under dark conditions, and could indicate several phenomena. First, the reformation of the electrochemical ionic bilayer after photocurrent generation could occur. Second, **UDS-6** may be inherently semi-conductive ($E_g < 2$ eV) and allow some current to pass, even at low potentials relative to NHE. This is corroborated by the small negative current displayed in the CV profiles of **UDS-6** in the same experimental setup (Figure S28).

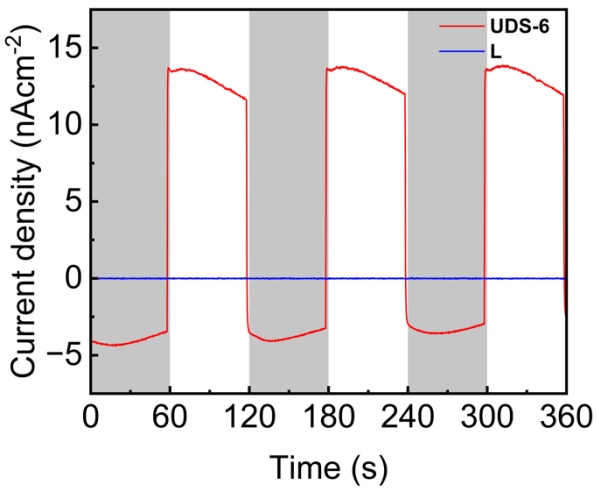

Figure 9. Photocurrent density for **UDS-6** and **L** under dark and light conditions. A significant difference in current density is found for **UDS-6** between dark and light conditions. Shaded areas correspond to dark periods, and white areas correspond to light irradiation periods.

Except for several CuX-based CPs used in DSSCs, it is noteworthy that no investigations were conducted on the inherent photoconductivity of this kind of material.[19,21,22] When comparing to the current produced by the herein mentioned DSSCs (in the range of 10^{-4} Acm^{-2}), the current generated by **UDS-6** is rather modest, but the large differences are expected since DSSCs are heterogeneous in nature, while **UDS-6** is a homogeneous material. It is also important to stress the fact that photoluminescence and photoconductivity are incompatible as photo-induced electron transfer generate optically silent radical species. So, considering this property and the arguments provided above, it is without a surprise that the anti-Kasha emission is found to be weak.

Rational design of a photoconductive material **UDS-6** was demonstrated by using the widely-known hole carrier CuBr, and the push-pull dye **L**, acting as the charge carrier. Their use in a CP material combined these known properties and gave the material auspicious properties and functionality. The further elaboration of this avenue for the rational design of photoconductive materials may involve different hole or charge carriers for increased performances.

3.6. Stability of UDS-6

The thermal, and photoelectrochemical stability of **UDS-6** were assessed to probe its applicability as a functional material. The thermogravimetric analysis (TGA) curve of **UDS-6** shows an important robustness, with first signs of degradation occurring over 200°C (Figure S29).

Moreover, cyclic voltammetry traces measured as a function of irradiance were also acquired. No significant difference in oxidation and reduction peaks between both conditions (Figure S28) was observed, indicating that there is no chemical change in the material upon irradiation, but that the excited **UDS-6** material itself is intrinsically responsible for the photocurrent.

Finally, **UDS-6** was soaked in the 0.5 M aqueous sodium sulfate environment used for electrochemical characterizations for one hour, and its measured PXRD pattern after soaking shows that crystallinity and identity is retained after this manipulation (Figure S30). This stability of **UDS-6** contrasts with many Cu(I) species, which tend to readily oxidate in aqueous media. This may be due to the hydrophobic shielding provided by the various **L** fragments around the nodes.

4. CONCLUSIONS

This work demonstrated that the rational design of a CP as a functional material from a basic pre-analysis of the component properties prior assembly is possible. Despite the relative paucity of literature on both components, it was possible to anticipate the outcome of the resulting CP beforehand, such as CT-type excited states, photoconductivity, and fabrication of a 1D- or 2D-network with a high probability. During this investigation, **UDS-6** turned out to be quite special on its own. The most striking property is the presence of a weak fluorescence even though this 2D-CP is photoconductive. The explanation may reside in the low population of the $[Cu_2Br_2]^{+\bullet}$/$[Cu_2Br_2]$ and $[\mathbf{L}]^{-\bullet}$/[**L**] species, which may be associated with the low photoconductivity of this material. The particularly low energy fluorescence process where the band is entirely located within the NIR region is rather scarce, and even particularly rare if this emission is also anti-Kasha. The low fluorescence intensity is certainly associated with the auto-absorption phenomenon within the bulk accompanied by the presence of photoconductivity. Finally, the presence of excitation energy migration is not uncommon, but the presence of inefficient and active sites for energy transfers within the same material is also interesting. Based on the Förster theory, it was possible to reliably

propose that the interlayer exciton migration is the dominant mechanism for singlet-singlet annihilation. The rational design of further such materials will lie in the full exploitation of the known properties of CPs based on similar motifs. The exploitation of exciton migration, broad-band absorbance, and combination of optimal photoelectrochemical agents will allow for the rational optimization of photocurrent performances in coordination polymers.

AUTHOR CONTRIBUTIONS

LB : Conceptualization, data curation, formal analysis, investigation, methodology, project administration, validation, visualization, writing – original draft, writing – review & editing.

EVD : Formal analysis, investigation, methodology, validation, writing – original draft, writing – review & editing.

AS : Formal analysis, investigation, methodology, validation.

DF : Formal analysis, investigation, methodology, validation.

PLK : Formal analysis, investigation, methodology, validation.

CL : Funding acquisition, resources, supervision.

PDD : Funding acquisition, resources, supervision, validation.

PDH : Formal analysis, funding acquisition, project administration, resources, supervision, validation, writing – original draft, writing – review & editing.

ACKNOWLEDGEMENTS

LB, and PDH acknowledge the financial support of the Université de Sherbrooke, and of the Natural Sciences and Engineering Research Council of Canada (CRSNG-NSERC). These authors further acknowledge the support of Calcul Québec and the Alliance de la Recherche Numérique du Canada given for this work.

EVD, and PDD acknowledge acknowledge financial support from a Vanier Scholarship and the NSERC Discovery program.

AS, and CL acknowledge the support of the CNRS, the French “Ministère de l’Enseignement Supérieur, de la Recherche et de l’Innovation” .

LB wishes to thank Pr. Yue Zhao, Ph.D. for access to his UV-Vis-NIR spectrophotometer, as well as Mr. Jérémy Baribeault, B. Sc. for technical support on this instrument. LB further wishes to thank Pr. Jérôme Claverie, Ph.D. for access to his light-dependent voltammeter, as well as Ms. Peipei Liu, M.Sc. for technical support on this instrument.

REFERENCES

1 P. Mondal and S. P. Rath, *Chem Eur J*, 2016, 22, 5607–5619.

2 P. Mondal and S. P. Rath, *Isr J Chem*, 2016, 56, 144–155.

3 R. O. Loutfy, C. K. Hsiao, B. S. Ong and B. Keoshkerian, *Can J Chem*, 1984, 62, 1877–1885.

4 A. D. Finke, B. O. Jahn, A. Saithalavi, C. Dahlstrand, D. Nauroozi, S. Haberland, J. Gisselbrecht, C. Boudon, E. Mijangos, W. B. Schweizer, S. Ott, H. Ottosson and F. Diederich, *Chem Eur J*, 2015, 21, 8168–8176.

5 C. Hubert, K. Tran, F. Hauquier, C. Cougnon, J.-F. Pilard, P. Gosselin, J. Rault-Berthelot and E. Raoult, *New J Chem*, 2007, 31, 1730.

6 J. Rault-Berthelot and E. Raoult, *Adv Mater Opt Electron*, 2000, 10, 267–272.

7 T. Senga, K. Kamoshida, L. A. Kushch, G. Saito, T. Inayoshi and I. Ono, *Mol Cryst Liq Cryst*, 1997, 296, 97–143.

8 G. Sbrana, M. Scotton and L. Angeloni, *J Chem Soc, Perkin Trans 2*, 1982, 1611.

9 S. Vallejos, H. El Kaoutit, P. Estévez, F. C. García, J. L. de la Peña, F. Serna and J. M. García, *Polym Chem*, 2011, 2, 1129–1138.

10 B. Kubendiran, G. Pramanik and G. K. Kole, *J Mol Struct*, 2023, 1294, 136397.

11 L. A. Estrada, A. Francés-Monerris, I. Schapiro, M. Olivucci and D. Roca-Sanjuán, *Phys Chem Chem Phys*, 2016, 18, 32786–32795.

12 J. Rault-Berthelot and C. Rozé, *J Chim Phys Physicochim Biol*, 1998, 95, 1188–1191.

13 B. Centrella, G. Deplano, A. Damin, M. Signorile, M. Tortora, C. Barolo, M. Bonomo and S. Bordiga, *Dalton Trans*, 2022, 51, 14439–14451.

14 M. Knorr, A. Khatyr, A. Dini Aleo, A. El Yaagoubi, C. Strohmann, M. M. Kubicki, Y. Rousselin, S. M. Aly, D. Fortin, A. Lapprand and P. D. Harvey, *Cryst Growth Des*, 2014, 14, 5373–5387.

15 Y. Liao, L. Shi, J. Feng, L. Yang and A. Ren, *Chem Res Chin Univ*, 2007, 23, 92–95.

16 Y. Liao, L.-L. Shi, J.-K. Feng, L. Yang and A.-M. Ren, *J Theor Comput Chem*, 2006, 05, 401–409.

17 A. Schlachter, K. Tanner and P. D. Harvey, *Coord Chem Rev*, 2021, 448, 214176.

18 A. Schlachter and P. D. Harvey, *J Mater Chem C*, 2021, 9, 6648–6685.

19 T. Zhou, C. Zhang, Z. Zhang, Y. Zhang and Y. Xiao, *Z Anorg Allg Chem*, 2021, 647, 2219–2225.

20 T. Okubo, N. Tanaka, K. H. Kim, H. Yone, M. Maekawa and T. Kuroda-Sowa, *Inorg Chem*, 2010, 49, 3700–3702.

21 H. Michaels, M. J. Golomb, B. J. Kim, T. Edvinsson, F. Cucinotta, P. G. Waddell, M. R. Probert, S. J. Konezny, G. Boschloo, A. Walsh and M. Freitag, *J Mater Chem A*, 2022, 10, 9582–9591.

22 S.-Q. Bai, I. H. K. Wong, N. Zhang, K. Lin Ke, M. Lin, D. J. Young and T. S. A. Hor, *Dalton Trans*, 2018, 47, 16292–16298.

23 A. Schlachter, P. Asselin, A. Chatelain and P. D. Harvey, *Adv Funct Mater*, , DOI:10.1002/adfm.202404111.

24 L. Boivin, A. Schlachter, D. Fortin, C. Lescop and P. D. Harvey, *Molecules*, 2023, 28, 7781–7799.

25 X. Yang, T. Fox and H. Berke, *Chem Comm*, 2011, 47, 2053.

26 M. Ghandi, S. J. Tabatabaei Rezaei, A. Yari and A. Taheri, *Tetrahedron Lett*, 2008, 49, 5899–5901.

27 G. M. Sheldrick, *Acta Crystallogr C Struct Chem*, 2015, 71, 3–8.

28 G. M. Sheldrick, *Acta Crystallogr A*, 2008, 64, 112–122.

29 O. V. Dolomanov, L. J. Bourhis, R. J. Gildea, J. A. K. Howard and H. Puschmann, *J Appl Crystallogr*, 2009, 42, 339–341.

30 H. Wang, S. Y. Sayed, E. J. Luber, B. C. Olsen, S. M. Shirurkar, S. Venkatakrishnan, U. M. Tefashe, A. K. Farquhar, E. S. Smotkin, R. L. McCreery and J. M. Buriak, *ACS Nano*, 2020, 14, 2575–2584.

31 M. J. Frisch, G. W. Trucks, H. E. Schlegel, G. E. Scuseria, M. A. Robb, Cheeseman. J. R., G. Scalmani, V. Barone, G. A. Petersson, F. O., J. B. Foresman and J. D. Fox, 2016.

32 N. M. O'boyle, A. L. Tenderholt and K. M. Langner, *J Comput Chem*, 2008, 29, 839–845.

33 S. Clément, S. Mohammed Aly, D. Fortin, L. Guyard, M. Knorr, A. S. Abd-El-Aziz and P. D. Harvey, *Inorg Chem*, 2008, 47, 10816–10824.

34 S. Clément, T. Goudreault, D. Bellows, D. Fortin, L. Guyard, M. Knorr and P. D. Harvey, *Chem Comm*, 2012, 48, 8640.

35 A. Langlois, J.-M. Camus, P.-L. Karsenti, R. Guilard and P. D. Harvey, *Inorg Chem*, 2017, 56, 2506–2517.

36 J.-M. Camus, A. Langlois, S. Aly, R. Guilard and P. D. Harvey, *J Porphyr Phthalocyanines*, 2013, 17, 722–732.

37 K. Momma and F. Izumi, *J Appl Crystallogr*, 2011, 44, 1272–1276.

38 M. A. Collins and R. P. A. Bettens, *Chem Rev*, 2015, 115, 5607–5642.

39 G. A. Dolgonos, O. A. Loboda and A. D. Boese, *J Phys Chem A*, 2018, 122, 708–713.

40 D. Piché and P. D. Harvey, *Can J Chem*, 1994, 72, 705–713.

41 F. Juvenal, H. Lei, A. Schlachter, P.-L. Karsenti and P. D. Harvey, *J Phys Chem C*, 2019, 123, 5289–5302.

42 F. Juvenal, H. Lei, P.-L. Karsenti and P. D. Harvey, *J Organomet Chem*, 2019, 896, 24–31.

43 A. Bonnot, P.-L. Karsenti, F. Juvenal, C. Golz, C. Strohmann, D. Fortin, M. Knorr and P. D. Harvey, *Phys Chem Chem Phys*, 2016, 18, 24845–24849.

44 A. Schlachter, A. Bonnot, D. Fortin, P.-L. Karsenti, M. Knorr and P. D. Harvey, *Phys Chem Chem Phys*, 2019, 21, 16538–16548.

45 J. R. Lakowicz, in *Principles of Fluorescence Spectroscopy*, Springer US, Boston, MA, 2006, pp. 443–475.

46 G. P. Kissling, B. Ruhstaller and K. P. Pernstich, *Org Electron*, 2023, 122, 106888.

47 R. S. Nicholson, *Anal Chem*, 1965, 37, 1351–1355.

48 L. R. Faulkner, H. S. White and A. J. Bard, *Electrochemical Methods : Fundamentals and Applications*, Wiley, 3rd edn., 2022.

49 R. A. Marcus, *Can J Chem*, 1959, 37, 155–163.